

# High-frame-rate echocardiography using diverging transmit beams and parallel receive beamforming

Hideyuki Hasegawa · Hiroshi Kanai

Received: 23 February 2011 / Accepted: 20 March 2011  
© The Japan Society of Ultrasonics in Medicine 2011

## Abstract

**Purpose** Echocardiography is a widely used modality for diagnosis of the heart. It enables observation of the shape of the heart and estimation of global heart function based on B-mode and M-mode imaging. Subsequently, methods for estimating myocardial strain and strain rate have been developed to evaluate regional heart function. Furthermore, it has recently been shown that measurements of transmural transition of myocardial contraction/relaxation and propagation of vibration caused by closure of a heart valve would be useful for evaluation of myocardial function and viscoelasticity. However, such measurements require a frame rate much higher than that achieved by conventional ultrasonic diagnostic equipment. In the present study, a method based on parallel receive beamforming was developed to achieve high-frame-rate (over 300 Hz) echocardiography.

**Methods** To increase the frame rate, the number of transmits was reduced to 15 with angular intervals of  $6^\circ$ , and 16 receiving beams were created for each transmission to obtain the same number and density of scan lines as realized by conventional sector scanning. In addition, several transmits were compounded to obtain each scan line to reduce the differences in transmit–receive sensitivities among scan lines. The number of transmits for compounding was determined by considering the width of the transmit beam. For transmission, plane waves and diverging waves were investigated. Diverging waves

showed better performance than plane waves because the widths of plane waves did not increase with the range distance from the ultrasonic probe, whereas lateral intervals of scan lines increased with range distance.

**Results** The spatial resolution of the proposed method was validated using fine nylon wires. Although the widths at half-maxima of the point spread functions obtained by diverging waves were slightly larger than those obtained by conventional beamforming and parallel beamforming with plane waves, point spread functions very similar to those obtained by conventional beamforming could be realized by parallel beamforming with diverging beams and compounding. However, there was an increase in the lateral sidelobe level in the case of parallel beamforming with plane and diverging waves. Furthermore, the heart of a 23-year-old healthy male was measured.

**Conclusion** Although the contrast of the B-mode image obtained by the proposed method was degraded due to the increased sidelobe level, a frame rate of 316 Hz, much higher than that realized by conventional sector scanning of several tens of Hertz, was realized with a full lateral field of view of  $90^\circ$ .

**Keywords** Diverging beam · Parallel beam forming · High-frame-rate imaging · Echocardiography

## Introduction

Echocardiography is one of the predominant modalities for diagnosis of the heart because it provides a cross-sectional image of the heart noninvasively in real time. Owing to the high temporal resolution of ultrasonic diagnostic equipment, global heart function, such as ejection fraction (EF), can be estimated based on B-mode and M-mode imaging

H. Hasegawa (✉) · H. Kanai  
Graduate School of Biomedical Engineering, Tohoku University,  
Aramaki-aza-Aoba 6-6-05, Aoba-ku, Sendai 980-8579, Japan  
e-mail: hasegawa@ecei.tohoku.ac.jp

H. Hasegawa · H. Kanai  
Graduate School of Engineering, Tohoku University,  
Aramaki-aza-Aoba 6-6-05, Aoba-ku, Sendai 980-8579, Japan

much more easily compared with other diagnostic modalities, such as magnetic resonance imaging (MRI) or computed tomography (CT). To evaluate regional myocardial function quantitatively, methods for measurements of myocardial strain and strain rate have been developed [1–3]. These methods enable estimation of regional deformation of the heart wall based on measurements of movement. Although measured strain and strain rate themselves are useful for evaluation of regional myocardial function, it has recently been shown that measurements of transmural transition of myocardial contraction/relaxation and propagation of vibration caused by closure of a heart valve would be useful for evaluation of myocardial function and viscoelasticity [4–6]. However, such measurements require a frame rate much higher than that achieved by conventional ultrasonic diagnostic equipment; for example, electrical excitation propagates in Purkinje fibers and ventricular muscle at typical velocities of 0.3–4 m/s [7], and corresponding propagation velocities of myocardial contraction of 0.5–7 m/s were measured by ultrasound [5, 8]. A high frame rate, typically higher than 200 Hz, which is much higher than that realized by conventional ultrasonic diagnostic equipment of several tens of Hertz, is required to measure the propagation of this electromechanical wave and the resulting transient small motion of the heart wall.

Konofagou et al. [9] and D’hooge et al. [10] increased the frame rate to above 200 Hz by reducing the size of the field of view and the total number of scan lines in an ultrasonic image. Furthermore, Konofagou et al. introduced an electrocardiogram (ECG)-gating technique in ultrasound imaging to combine individual small sectors into a large field of view [11]. In this method, the lateral size of a sector (corresponding to the number of scan lines) obtained in one acquisition is narrowed to achieve a higher frame rate of about 500 Hz. By measuring a number of small sectors during the corresponding number of cardiac cycles, the measured small sectors are combined into a large sector format based on ECG gating. Although this method achieves a frame rate of about 500 Hz, which is much higher than the conventional frame rate of several tens of Hertz, measurements for a number of cardiac cycles are required.

To achieve a high frame rate of about 500 Hz without ECG gating, we used sparse sector scanning, in which the number of scan lines was decreased to about 10 [12]. In this method, the angle intervals between scan lines are increased to obtain a large lateral field of view with a small number of scan lines. Therefore, the lateral image resolution is significantly degraded.

The above-mentioned methods are based on conventional beamforming. Therefore, they need to sacrifice the

density of scan lines or field of view to achieve a high frame rate. To overcome this problem, parallel receive beamforming with a wide transmit beam has been developed [13] to illuminate a wider region by one transmission to reduce the number of transmissions. This could be done in the cited study by conventional transmit beamforming (focusing at a certain range distance) because such beams are wide in the region shallower than the focal distance (between the transducer surface and the focal point). Using this method, real-time three-dimensional (3D) imaging of the heart was realized at a frame rate of a few tens of Hertz. However, the width of the transmit beam is narrower than the size of the aperture, and this would limit the number of receiving beams created by one transmission.

Lu et al. [14–17] proposed an alternative imaging method using an unfocused but nondiverging transmit beam, namely, a limited diffraction beam. Unfocused beams achieved a wider beam width, and nondiverging beams used in these cited studies preventinsonified energy from being spread to assure the required penetration depth. However, the width of a nondiverging beam is still limited by the size of the aperture.

On the other hand, diverging beams have potential to enlarge the region illuminated by one transmission. In synthetic-aperture ultrasound imaging, a single element or a small number of elements are used to produce spherical waves [21, 22]. Although a spherical wave can illuminate a wide area by one transmission, acoustic pressure significantly decreases with propagation distance, and the signal-to-noise ratio (SNR) of the received signal would be significantly reduced.

In the present study, the feasibility of using a diverging transmit beam in ultrasonic imaging with parallel beamforming [18–20] was investigated to achieve a frame rate above 200 Hz with adequate lateral spatial resolution, wider field of view, and no ECG gating. Diverging waves can be produced by using all transducer elements in an ultrasonic array probe to obtain ultrasonic echoes with better SNR [23]. The width of the diverging angle was limited to suppress the decay of acoustic pressure due to the propagation distance. Furthermore, the diverging beam was steered to obtain an ultrasonic image of a heart with a full angle of 90° with a limited beam width. To increase the frame rate, the number of transmits was reduced to 15 with a transmit angular interval of 6°, and 16 receiving beams were created in each transmit to obtain the same number and density of scan lines as realized by conventional sector scanning. The spatial resolution of the proposed imaging method was evaluated by basic experiments using fine nylon wires. Furthermore, B-mode images of the heart of a 23-year-old healthy male measured by the proposed method were obtained.

**Materials and methods**

**Mathematical description of ultrasound waves emitted from transducer elements**

Let us describe ultrasound waves emitted from transducer elements of a phased-array ultrasonic probe. To achieve a frame rate over 200 Hz under a typical pulse repetition frequency of 5 kHz (realized by the ultrasound system used in the present study with an observation range setting of 130 mm), the number of transmits should be <25. Therefore, in the present study, plane waves or diverging waves were transmitted in 15 directions  $\{m\Theta\} (m = -7, -6, \dots, 0, 1, \dots, 7)$  with angular intervals of  $\Theta = 6^\circ$ . The ultrasonic wave  $g_{i,m}(\mathbf{p}; t)$  at time  $t$  from the time of transmission, which is emitted from the  $i$ th transducer element ( $i = 0, 1, \dots, L - 1$ ) in the  $m$ th transmission and insonifies to a spatial point  $\mathbf{p} = (r, \theta)$ , as shown in Fig. 1, is expressed as follows:

$$g_{i,m}(\mathbf{p}; t) = s_i(t - \tau_{t,i,m}(\mathbf{p})), \tag{1}$$

where  $s_i(t)$  is the impulse response of the  $i$ th transducer element, and  $\tau_{t,i,m}(\mathbf{p})$  is the time delay due to propagation of an ultrasonic wave from the  $i$ th element to the spatial point  $\mathbf{p}$ . The time delay  $\tau_{t,i,m}(\mathbf{p})$  of  $g_{i,m}(\mathbf{p}; t)$  is given by

$$\tau_{t,i,m}(\mathbf{p}) = \frac{\sqrt{r^2 \cos^2 \theta + \left\{ r \sin \theta - \left(i - \frac{L-1}{2}\right) \Delta x \right\}^2}}{c_0} + T_{\text{TBF},i,m}, \tag{2}$$

where  $\Delta x$  and  $c_0$  are the lateral pitch of transducer elements and speed of sound, respectively, and  $T_{\text{TBF},i,m}$  is the time

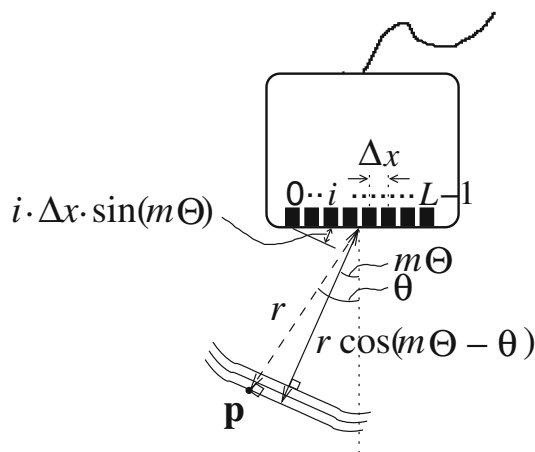


**Fig. 1** Illustrations of a plane wave insonifying to spatial point  $\mathbf{p} = (r, \theta)$  and propagation distance  $r \cos(m\Theta - \theta)$  required to illuminate spatial point  $\mathbf{p}$ , which is located at distance  $r$  from the center of the array, using a plane wave

delay applied to the  $i$ th element in the  $m$ th transmission by the transmit beamformer.

To emit a plane wave at steering angle of  $m\Theta$ ,  $T_{\text{TBF},i,m}$  should be given by

$$T_{\text{TBF},i,m} = \begin{cases} \frac{i \cdot \Delta x \cdot \sin(m\Theta)}{c_0} & \text{if } m \geq 0, \\ \frac{(i-L+1) \cdot \Delta x \cdot \sin(m\Theta)}{c_0} & \text{if } m < 0. \end{cases} \tag{3}$$

$(i = 0, 1, \dots, L - 1)$

The time delay  $T_{\text{TBF},i,m}$  applied by the transmit beamformer is greater than or equal to zero.

For a circular planar transducer, the Fresnel zone (range of near field) is defined by the diameter of the aperture  $D$  and the ultrasonic wavelength  $\lambda$  as  $D^2/(4\lambda)$ . The aperture width  $D$  of the sector probe and the ultrasonic wavelength  $\lambda$  used in the present study were about 20 mm and about 0.4 mm (center frequency 3.75 MHz), respectively. Although the phased-array probe used in the present study was not circular, the range of near field can be approximately obtained based on this equation. The range of the Fresnel zone of the probe used was 250 mm, and thus a range of about 130 mm, which was imaged in the present study, was included in the near field. In the near field, the width of a plane wave is constant. On the other hand, in ultrasonic imaging in sector format, the lateral width of a small sector imaged by one transmission increases with range distance, and thus the performance of a plane wave would be limited because the lateral width of a plane wave does not increase with range distance in the near field.

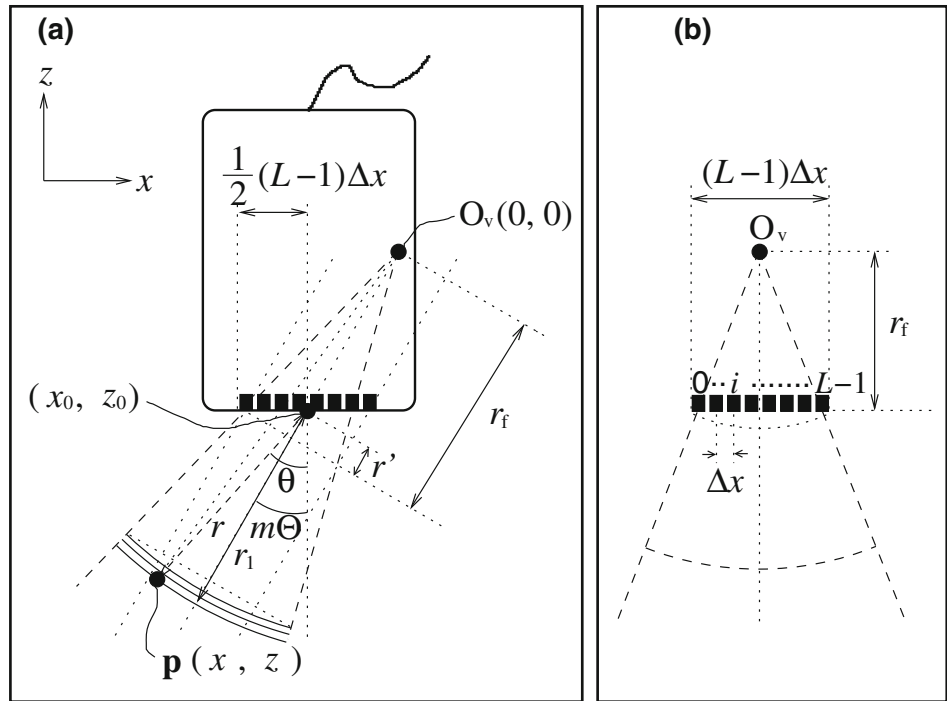
To solve this problem, in the present study a diverging wave, illustrated in Fig. 2a, was used for transmission in addition to a plane wave. In synthetic-aperture imaging, each element is individually used to emit a spherical wave. Such diverging waves would be useful for ultrasonic imaging in sector format. However, the intensity of the emitted wave would significantly decrease because a single element is used. Alternatively, spherically diverging waves [22] can be produced using all the transducer elements in every transmission. In the present study, such a diverging wave was realized by applying a time delay  $T_{\text{TBF},i,m}$  to the  $i$ th transducer element in the  $m$ th transmission, given by

$$T_{\text{TBF},i,m} = \begin{cases} \frac{i \cdot \Delta x \cdot \sin(m\Theta)}{c_0} + \frac{\sqrt{\left\{ \left(i - \frac{L-1}{2}\right) \Delta x \right\}^2 + r_f^2} - r_f}{c_0} & \text{if } m \geq 0, \\ \frac{(i-L+1) \cdot \Delta x \cdot \sin(m\Theta)}{c_0} + \frac{\sqrt{\left\{ \left(i - \frac{L-1}{2}\right) \Delta x \right\}^2 + r_f^2} - r_f}{c_0} & \text{if } m < 0, \end{cases} \tag{4}$$

$(i = 0, 1, \dots, L - 1)$

where  $r_f$  is the distance from a virtual point source  $O_v$  behind the array to the surface of the transducer array. The first term in the right-hand side of Eq. 4 is required to steer the direction of the transmit beam to  $m\Theta$ . The second term, which is required to realize a diverging

**Fig. 2** Illustration of a diverging wave. **a** Propagation distance  $r_1$  required to illuminate spatial point  $\mathbf{p}$ , which is located at distance  $r$  from the center of the array, using a diverging wave. **b** Geometry for consideration of time delays applied to transducer elements for diverging wave transmission



wave, was obtained in the present study by considering the geometry illustrated in Fig. 2b. The second term depends on the distance from the virtual point source  $O_v$  to the  $i$ th element in Fig. 2b.

Parallel receive beamforming

In this study, ultrasonic beams (plane or diverging waves) emitted in 15 directions at angle intervals of  $\Theta = 6^\circ$  and 16 receiving beams with angle intervals of  $0.375^\circ$  were created for each transmit to realize a similar number and density of scan lines as obtained by conventional sector scanning. The value,  $\widehat{O}_m(\mathbf{p})$ , of the beamformed radio frequency (RF) signal at a spatial point  $\mathbf{p}$  is generated from ultrasonic echo signals  $\{y_{i,m}(t)\}$  received by the elements ( $i = 0, 1, \dots, L - 1$ ), which contain echoes scattered at all points illuminated by the  $m$ th transmission, as follows:

$$\widehat{O}_m(\mathbf{p}) = \sum_{i=0}^{L-1} w_{r,i} \cdot y_{i,m}(t - \tau_{\text{RBF},i,m}(\mathbf{p})), \tag{5}$$

where  $w_{r,i}$  ( $i = 0, 1, \dots, L - 1$ ) corresponds to the receive apodization, and  $\tau_{\text{RBF},i,m}(\mathbf{p})$  is the time delay which should be applied by a receive beamformer to compensate the propagation delay of the emitted wave from the probe to  $\mathbf{p}$  and that of the scattered wave from  $\mathbf{p}$  to the  $i$ th element. The time delay  $\tau_{\text{RBF},i,m}(\mathbf{p})$ , which was applied by the receive beamformer to echo signal  $y_{i,m}(t)$  received by the  $i$ th element, is given by

$$\tau_{\text{RBF},i,m}(\mathbf{p}) = T_{\text{TW},m}(\mathbf{p}) + \frac{\sqrt{r^2 \cos^2 \theta + \{r \sin \theta - \Delta x(i - \frac{L-1}{2})\}^2}}{c_0}. \tag{6}$$

The second term of Eq. 6 corresponds to the propagation delay of a scattered echo from the spatial point  $\mathbf{p}$  to the  $i$ th element. The first term,  $T_{\text{TW},m}(\mathbf{p})$ , of Eq. 6 corresponds to the propagation delay of the emitted ultrasonic wave to spatial point  $\mathbf{p}$ , which depends on the receiving beam angle  $\theta$ . In the present study, as illustrated in Fig. 1, for a plane wave,  $T_{\text{TW},m}(\mathbf{p})$  was assigned as follows:

$$T_{\text{TW},m}(\mathbf{p}) = \frac{r \cos(\theta - m\Theta)}{c_0}. \tag{7}$$

For diverging waves, as illustrated in Fig. 2b,  $T_{\text{TW},m}(\mathbf{p})$  was assigned as follows:

$$T_{\text{TW},m}(\mathbf{p}) = \frac{\sqrt{x^2 + z^2} - r_f + r'}{c_0}, \tag{8}$$

$$x = r_f \sin(m\Theta) - r' \sin(m\Theta) + r \sin \theta, \tag{9}$$

$$z = -r_f \cos(m\Theta) + r' \cos(m\Theta) - r \cos \theta, \tag{10}$$

$$r' = \frac{1}{2} \cdot (L - 1) \cdot \Delta x \cdot \sin(m\Theta), \tag{11}$$

where  $(x, z)$  is the position of  $\mathbf{p}$  in Cartesian coordinates.

By changing  $\theta((m - 0.5) \cdot \Theta \leq \theta < (m + 0.5) \cdot \Theta)$  at intervals of  $0.375^\circ$  at each range position  $r$  in each of the  $m$

transmissions, beamformed RF signals  $\{\widehat{O}_m(\mathbf{p})\}$  at all spatial points  $\{\mathbf{p} = (r, \theta)\}$  in the field of view are obtained.

**Problem in parallel beamforming with phased array**

To obtain an ultrasonic image in sector format, ultrasonic beams need to be steered. Therefore, the directivity of the ultrasound beam changes depending on the steering angle. In receive beamforming, the difference between the directivities of neighboring receiving beams is not so significant because the angle intervals of receiving beams are small ( $0.375^\circ$ ). However, such difference is significant in transmission because of the relatively large angle interval of neighboring transmit beams of  $6^\circ$  (used in the present study). This significant change in directivity in transmission produces discontinuities in a resultant ultrasonic image at a pitch of  $6^\circ$ , which corresponds to angular intervals of transmit beams, because the transmit–receive directivity is defined by the product of the transmit and receive directivities [24]. Figure 3 shows a B-mode image of the heart of a 23-year-old healthy male, which was obtained using parallel beam forming expressed by Eq. 5 with plane wave transmission. As can be seen in Fig. 3, there are significant discontinuities at the edges of each region imaged by one transmission.

**Spatial compounding of multiple transmits in receive beamforming**

As described in the previous section, there are discontinuities in the ultrasound image when each scan line is created by a single transmission, because the lateral intensity profiles of transmit beams significantly differ between transmissions due to the large angular interval of transmit beams (in general, the intensity is decreased by

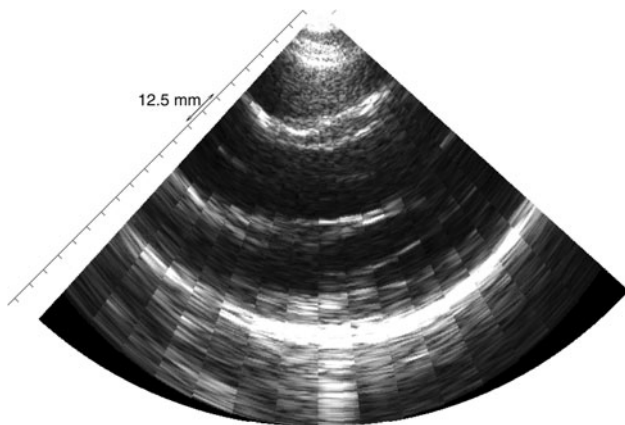


**Fig. 3** Longitudinal B-mode image of the heart of a 23-year-old male obtained by parallel beamforming without spatial compounding

steering due to the directivities of the transducer elements). Such discontinuities consist of high spatial (angular) frequency components, which degrade the image quality. A simple way to reduce such discontinuities (high spatial frequency components) in an ultrasound image obtained by parallel beamforming is to use spatial moving average, i.e., low-pass filtering. The spatially averaged beamformed RF signal  $\widehat{O}_s(r, \theta)$  at a spatial point  $\mathbf{p} = (r, \theta)$  is expressed as follows:

$$\widehat{O}_s(r, \theta) = \sum_{j=-M_s}^{M_s} w_j \cdot \widehat{O}_{m_0}(r, \theta + \Theta \cdot j) = \sum_{j=-M_s}^{M_s} w_j \cdot \widehat{O}_{m_0}(r, \theta + \Theta \cdot j) \cdot \exp\{-j2\pi f_\theta(\Theta \cdot j)\} \Big|_{f_\theta=0}, \tag{12}$$

where the number of averaged signals is expressed by  $(2M_s + 1)$ ,  $w_j$  is a weighting function, and  $m_0$  is the transmission number that gives the minimum difference between the direction of transmission  $m\Theta$  and the direction  $\theta$  of point  $\mathbf{p} = (r, \theta)$ . As can be seen in Eq. 12, the moving average operation corresponds to a Fourier transform with respect to angular frequency  $f_\theta$  of zero. The spatial frequency spectrum obtained by Eq. 12 is expressed by the convolution of the spatial frequency characteristics of  $w_j$  and  $\widehat{O}_m(r, \theta)$ , and thus the spatial frequency characteristics of the low-pass filtering applied by the moving average operation is determined by that of the weighting function  $w_j$ . It is well known that a rectangular weighting function exhibits a higher sidelobe level in the frequency domain, which corresponds to higher leakage of high spatial frequency components. Therefore, a tapered function, such as a Hanning window, which exhibits lower sidelobe level, is preferable for the weighting function  $w_j$ .

Although the high spatial frequency components can be reduced by spatial averaging, the image would be blurred, because the beamformed RF signals  $\{\widehat{O}_m(\mathbf{p})\}$  at different spatial positions  $\{\mathbf{p}\}$  are averaged in Eq. 12. To avoid such blurring effect, in the present study, RF signals  $\{\widehat{O}_m(\mathbf{p})\}$  beamformed with respect to the same spatial position  $\mathbf{p}$  in different transmissions  $\{m\}$  are compounded. This procedure has a similar effect as Eq. 12, because the lateral intensity profiles of unfocused beams, such as plane wave and diverging wave, are almost homogeneous at every angle  $\theta$  within the beams. Therefore, we assumed that  $\widehat{O}_{m_0}(r, \theta + \Theta \cdot j) \approx \widehat{O}_{m_0+j}(r, \theta)$ .

By replacing the summation with respect to angle in Eq. 12 by that with respect to transmission, the compounded beamformed RF signal  $\widehat{O}_c(\mathbf{p})$  at  $\mathbf{p}$  is expressed as follows:

$$\widehat{O}_c(\mathbf{p}) = \sum_{j=-M_c}^{M_c} w_{c,m_0+j}(\mathbf{p}) \cdot \widehat{O}_{m_0+j}(\mathbf{p}), \tag{13}$$

where the number of compounded signals is expressed as  $(2M_c + 1)$ . In the present study, Hanning weighting was used in spatial compounded signals, expressed as follows:

$$w_{c,m}(\mathbf{p}) = \cos^2 \left\{ \frac{\pi}{2} \cdot \frac{(\theta - m\Theta)}{\frac{1}{2} \cdot (2M_c + 1)\Theta} \right\}, \tag{14}$$

where the number of compounded signals is expressed as  $(2M_c + 1)$ . In the present study,  $M_c$  was determined from the angular width of the emitted wave by considering the transducer geometry, as illustrated in Fig. 4. For plane waves, the angular width  $\theta_w$  at range distance  $r$  is given by

$$\theta_w = 2 \arctan \left( \frac{L \cdot \Delta x}{2r} \right). \tag{15}$$

For diverging waves, the diverging angle  $\phi$  is obtained as follows:

$$\phi = \arctan \left( \frac{L \cdot \Delta x}{2r_f} \right). \tag{16}$$

In the present study, using the diverging angle  $\phi$ , the lateral beam width  $l_w$  at range distance  $r$  is approximately given by

$$l_w = (r_f + r) \tan \phi. \tag{17}$$

The angular width  $\theta_w$  for a diverging wave is obtained as follows:

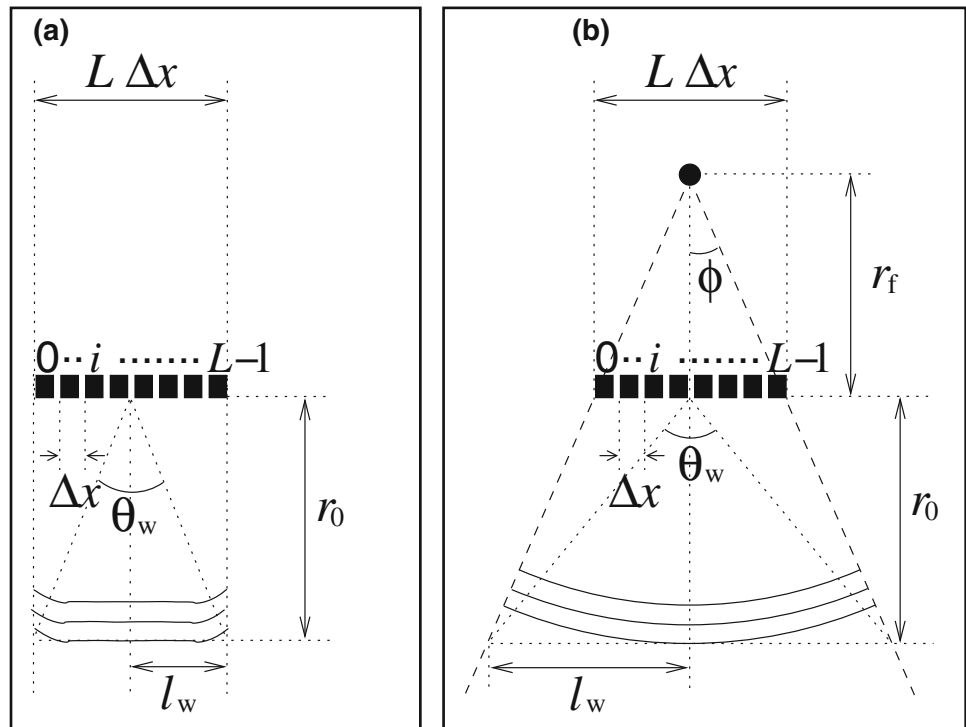
$$\theta_w = 2 \arctan \left( \frac{l_w}{r} \right). \tag{18}$$

The number of compounded signals  $(2M_c + 1)$  is determined so that the contribution of the emissions whose directions are different from the direction of interest  $\theta$  by larger than half the angular beam width  $\theta_w$  is gradually decreased. In the present study, this was given by  $(2M_c + 1)\Theta/2 < \theta_w$ . To satisfy this condition, the number of compounded signals was determined as follows:

$$M_c = \left\lfloor \frac{\theta_w}{\Theta} \right\rfloor. \tag{19}$$

In the present study, the angular beam width  $\theta_w$  was introduced to consider the relationship between the beam width and the interval of transmit beams, because sparser transmissions require a larger beam width to illuminate a larger region between the directions of successive transmissions. The angular beam width is more convenient than the beam width in distance, because the angular interval of transmit beams does not change with the range distance, whereas the interval in distance changes. In Fig. 5, angular widths  $\{\theta_w\}$  calculated for plane and diverging waves using Eqs. 15 and 18 are plotted as functions of range distance  $r$  (the aperture size  $L \cdot \Delta x = 19.2$  mm was the same as that of the ultrasonic probe used). The angular width  $\theta_w$  of a diverging wave at distance  $r_f$  from a virtual point source larger than 100 mm does not change so much compared with that of a plane wave. At the longest range distance of interest in the present study (130 mm), the angular width  $\theta_w$  doubles

**Fig. 4** Illustration of angular width  $\theta_w$  of emitted wave. **a** Plane wave. **b** Diverging wave



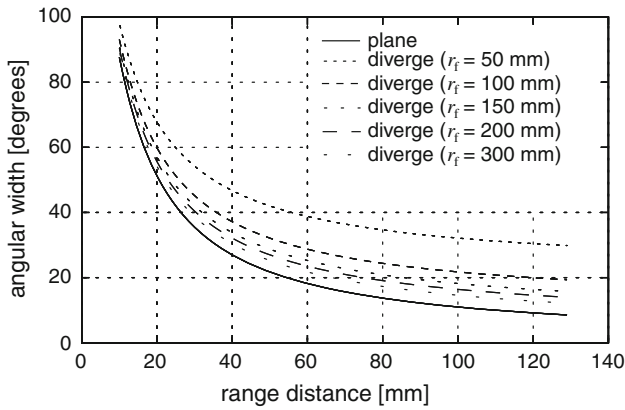


**Fig. 5** Angular widths  $\{\theta_w\}$  calculated for plane and diverging waves

at  $r_f = 100$  mm and triples at  $r_f = 50$  mm. The angular width  $\theta_w$  would further increase at smaller  $r_f$ . However, the intensity of the emitted wave would decrease further. Therefore, in the present study, diverging waves at  $r_f = 100$  and 50 mm are investigated in the subsequent sections.

**Evaluation of spatial resolution using a wire phantom**

In the present study, a commercial ultrasonic diagnostic system ( $\alpha$ -10; Aloka, Tokyo, Japan) was used with a 3.75-MHz phased-array probe. This system was modified so that RF echoes received by  $L = 96$  individual elements could be acquired at sampling frequency of 30 MHz for offline processing (receive beamforming, spatial compounding, etc.).

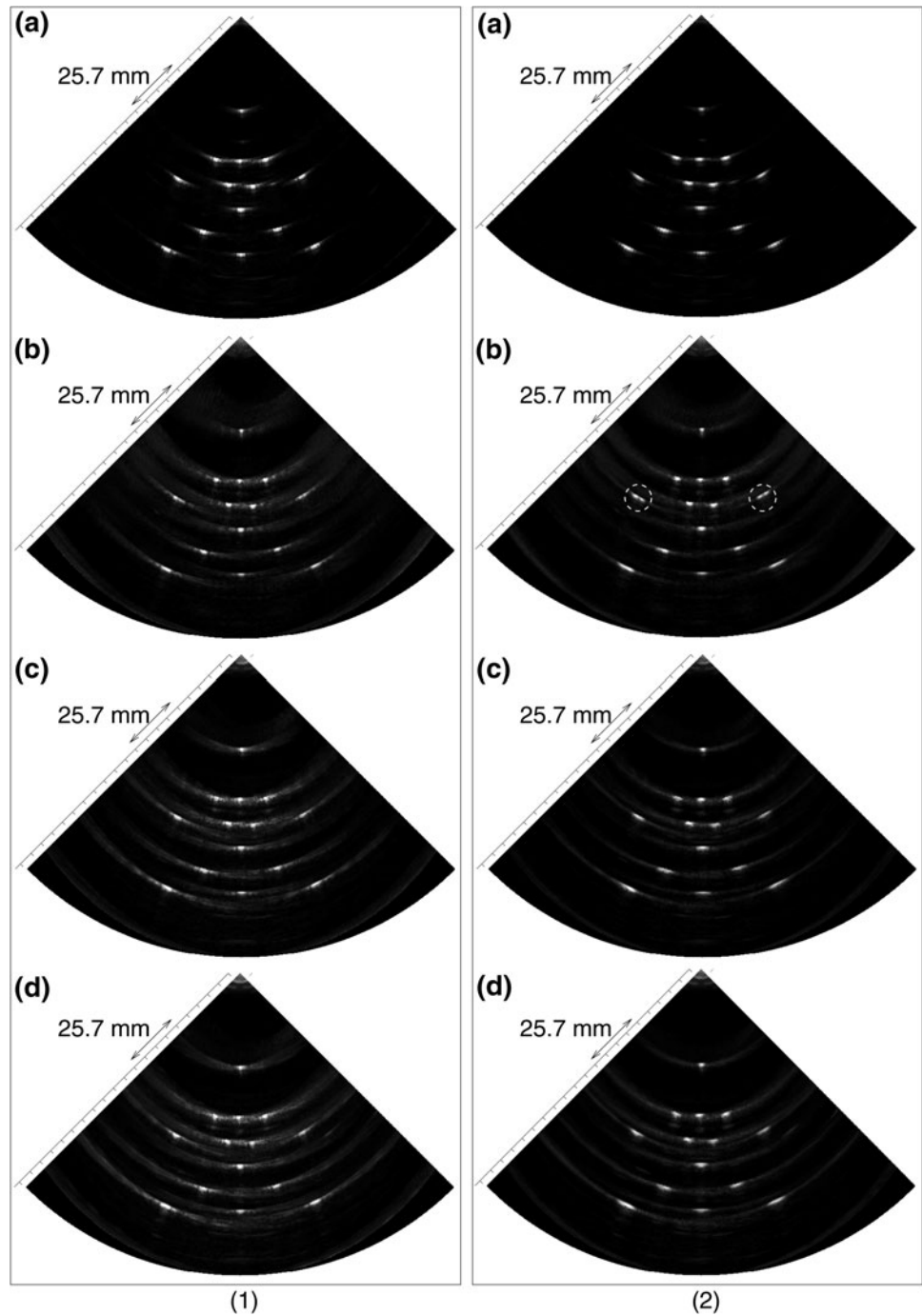
In the basic experiment, fine nylon wires (diameter  $\sim 100 \mu\text{m}$ ) placed in water were used for evaluation of the spatial resolution. Figure 6a–d shows B-mode images of the wires obtained by conventional sector scanning and parallel beamforming with spatial compounding using plane waves and diverging waves at  $r_f = 100$  and 50 mm, respectively. In Fig. 6(1) and (2), rectangular apodization ( $w_{r,i} = 1; i = 0, 1, 2, \dots, L - 1$ ) and Hamming apodization ( $w_{r,i} = 0.54 - 0.46 \cos(2\pi i/L); i = 0, 1, 2, \dots, L - 1$ ) were used, respectively. As can be seen in Fig. 6, the sidelobe levels significantly increased when rectangular apodization was used. Therefore, Hamming apodization was used in subsequent experiments.

In the B-mode image obtained by parallel beamforming with plane waves, the point spread function at larger steering angle (surrounded by white dashed lines in Fig. 6, 2b) was distorted (split in the lateral direction) because the widths of plane waves were narrow compared with diverging waves and the widths decreased when the steering angle was increased. Therefore, use of plane waves is limited to imaging at smaller steering angles. On the other hand, such distortion was not found in the B-mode images obtained by parallel beamforming with diverging waves.

Figure 7a, b shows axial and lateral profiles of the images (corresponding to point spread functions) at angular position  $\theta$  of  $0^\circ$  and range distance  $r$  of 41 mm, respectively. The widths at half-maxima of the point spread functions shown in Fig. 7 are presented in Table 1. As shown in Fig. 7, plane wave transmission achieved the best lateral spatial resolution. Although the widths at half-maxima of the point spread functions obtained by diverging waves were slightly larger than those obtained by conventional beamforming and parallel beamforming with plane waves, point spread functions very similar to those obtained by conventional beamforming could be realized by parallel beamforming with diverging beams and compounding. Figure 8a, b illustrates point spread functions created by compounding plane and diverging waves, respectively. The wavefronts and point spread functions shown by the dashed and solid lines illustrate those obtained by transmission at the lowest and the maximum steering angle in beamforming with respect to spatial point  $\mathbf{p}$ . The overlapping area of two point spread functions in Fig. 8 is enhanced in the resultant point spread function obtained by compounding. As can be seen in Fig. 8, the overlapping area obtained by plane waves is smaller than that obtained by diverging beams, even when the maximum steering angles are the same. Therefore, it was considered that plane wave transmission achieved the best lateral spatial resolution. However, there was an increase of the lateral sidelobe level with use of parallel beamforming with both plane and diverging waves. Although this increase of the sidelobe level would degrade image contrast, lateral spatial resolution comparable to that of conventional sector scanning was achieved by the proposed method.

In Fig. 7, the number of compounded signals ( $2M_c + 1$ ) was determined by Eq. 19. In Fig. 9(1) and (2),  $M_c$  was also determined by Eq. 19; however, the maximum  $M_c$  was limited to 4 and 2, respectively. For diverging waves, B-mode images obtained by limiting the maximum number of compounded signals were better than those obtained with unlimited  $M_c$ , as shown in Fig. 6. In the present study, the propagation delay of the emitted wave was calculated based on Eq. 8 without considering wavefront distortion due to beam steering. Therefore, it can be considered that a number of compounded signals  $M_c$  larger than 2 (corresponding to larger differences among the steering angles in emissions used for compounding) degraded the resultant images, because it would be difficult to estimate propagation delays at larger steering angles using Eq. 8 and the large number of transmissions (meaning a large difference among the angles of transmissions) used for compounding degrades coherent compounding. As in Fig. 7, Fig. 10 shows lateral profiles of envelopes of compounded beamformed RF echoes at range distance of 41 mm obtained by a diverging beam at  $r_f = 50$  mm with and without the

**Fig. 6** B-mode images of fine wires obtained by *a* conventional sector scanning and parallel beamforming using *b* plane waves, *c* diverging waves at  $r_f = 100$  mm, and *d* diverging waves at  $r_f = 50$  mm. **1** Rectangular and **2** Hamming apodizations were used



limitation  $M_c \leq 2$ . In Fig. 10, only profiles obtained with a diverging beam at  $r_f = 50$  mm are shown, because the number of compounded signals is largest among the transmit beams used in the present study. As shown in Fig. 10, degradation of coherent compounding reduces the difference between the main lobe and sidelobe levels and does not improve the spatial resolution. Consequently, in the present study, the number of compounded signals  $(2M_c + 1)$  was determined by Eq. 19; however, its maximum was restricted to be 5 for diverging waves.

In general, the insonified energy of a diverging wave spreads and acoustic intensity decreases with propagation distance. To reduce this decay, in the present study, the width of the diverging beam was limited. Figure 11 shows the axial profiles of the ultrasound images of the wire phantom (shown in Fig. 6) at lateral angle of  $0^\circ$ . As expected, the intensity at the deepest wire was strongest when focusing was done in both transmit and receive, as shown in Fig. 11. Although the intensity was lower than that obtained by focusing in both transmit and receive, the

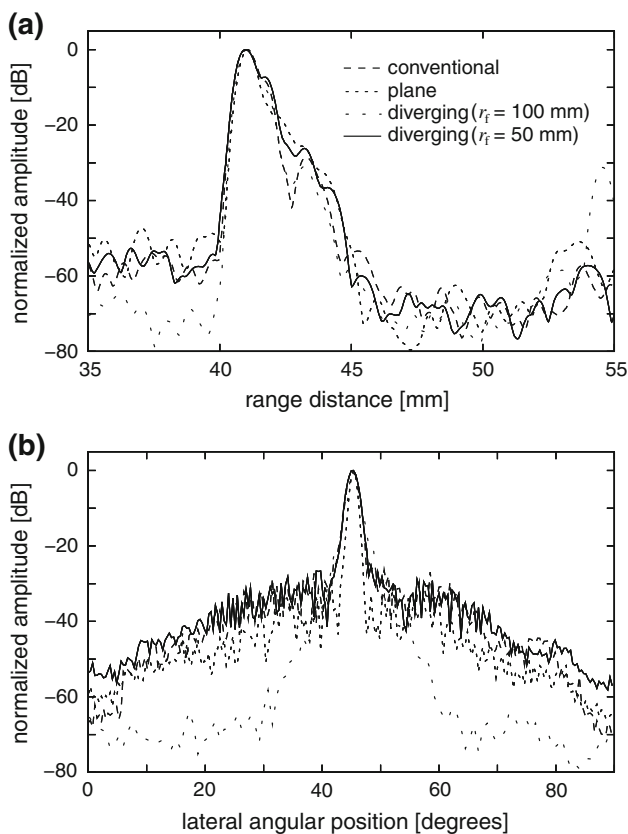


**Fig. 7** Axial and lateral profiles of envelopes of beamformed RF echoes obtained by respective methods. **a** Axial profile at lateral angular position of  $0^\circ$ . **b** Lateral profile at range distance of 41 mm

**Table 1** Widths at half-maxima of point spread functions shown in Fig. 7

	Conventional beamforming	Plane wave	Diverging wave ( $r_f = 100$ mm)	Diverging wave ( $r_f = 50$ mm)
Axial (mm)	0.73	0.71	0.88	0.84
Lateral (mm)	0.68	0.52	0.81	0.86

diverging waves used in the present study achieved decays of intensities (Fig. 11c, d) similar to those realized by plane waves (Fig. 11b).

**In vivo imaging of a human heart**

Figure 12a–d shows B-mode images of the heart of a 23-year-old healthy male obtained by conventional sector scan and parallel beamforming with plane waves and diverging waves at  $r_f = 50$  and 100 mm, respectively. The maximum of the number of compounded signals  $M_c$  was limited to 2 for diverging waves. Although a B-mode image of the heart could be obtained by plane wave transmission, the point spread function produced by

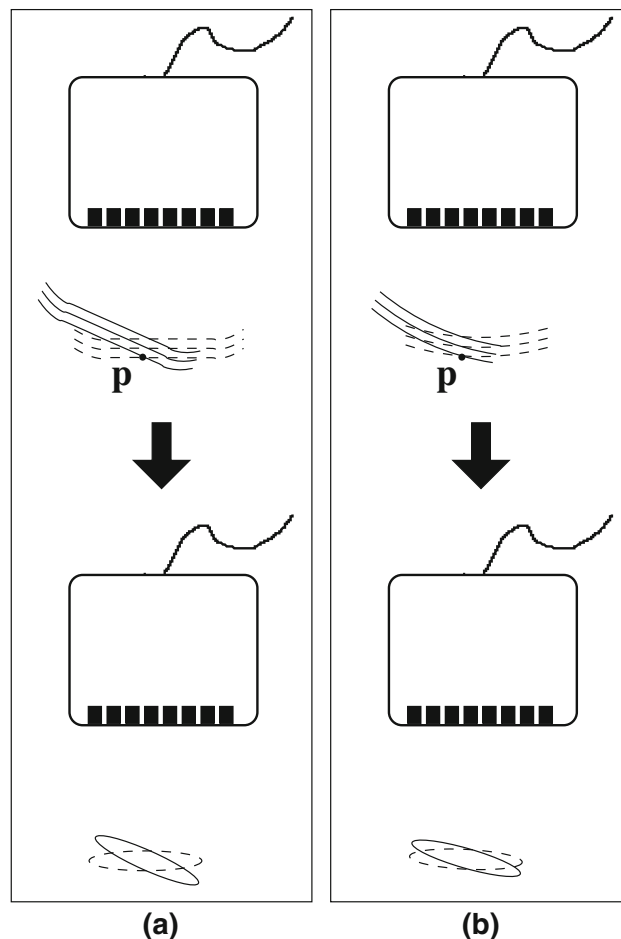


**Fig. 8** Wavefronts and point spread functions produced by **a** plane waves and **b** diverging waves

parallel beamforming with plane waves was split in the lateral direction, as shown in Fig. 6. Therefore, it might be better to use plane wave transmission with a smaller maximum steering angle. By using diverging waves, as shown in Fig. 12c, d, B-mode images of the heart could be obtained at a high frame rate of 316 Hz with a full lateral field of view of  $90^\circ$ , and the diverging waves at  $r_f = 50$  and 100 mm showed similar performance. Although image contrast was degraded due to the higher lateral sidelobe levels, a B-mode image with image quality comparable to that obtained by conventional sector scanning could be obtained at a frame rate (316 Hz) significantly higher than that (39 Hz) obtained by conventional sector scan, and a full field of view of  $90^\circ$  was achieved without requiring ECG gating [11].

**Discussion**

In the present study, a method based on parallel beamforming was investigated for high-frame-rate echocardiography. To

**Fig. 9** B-mode images of fine wires obtained by parallel beamforming with *a* plane waves, *b* diverging waves at  $r_f = 100$  mm, and *c* diverging waves at  $r_f = 50$  mm. The maximum number of compounded signals was constrained to be 1 4 and 2 2

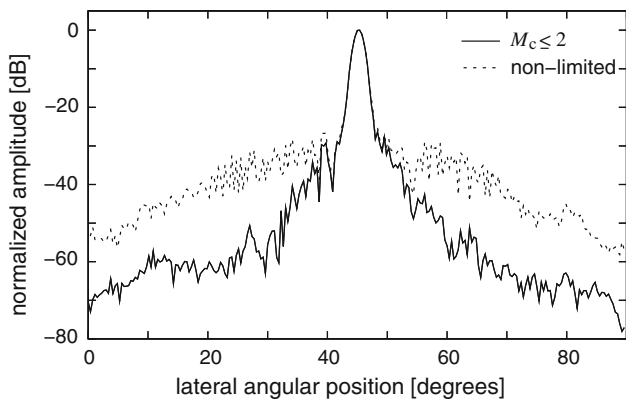
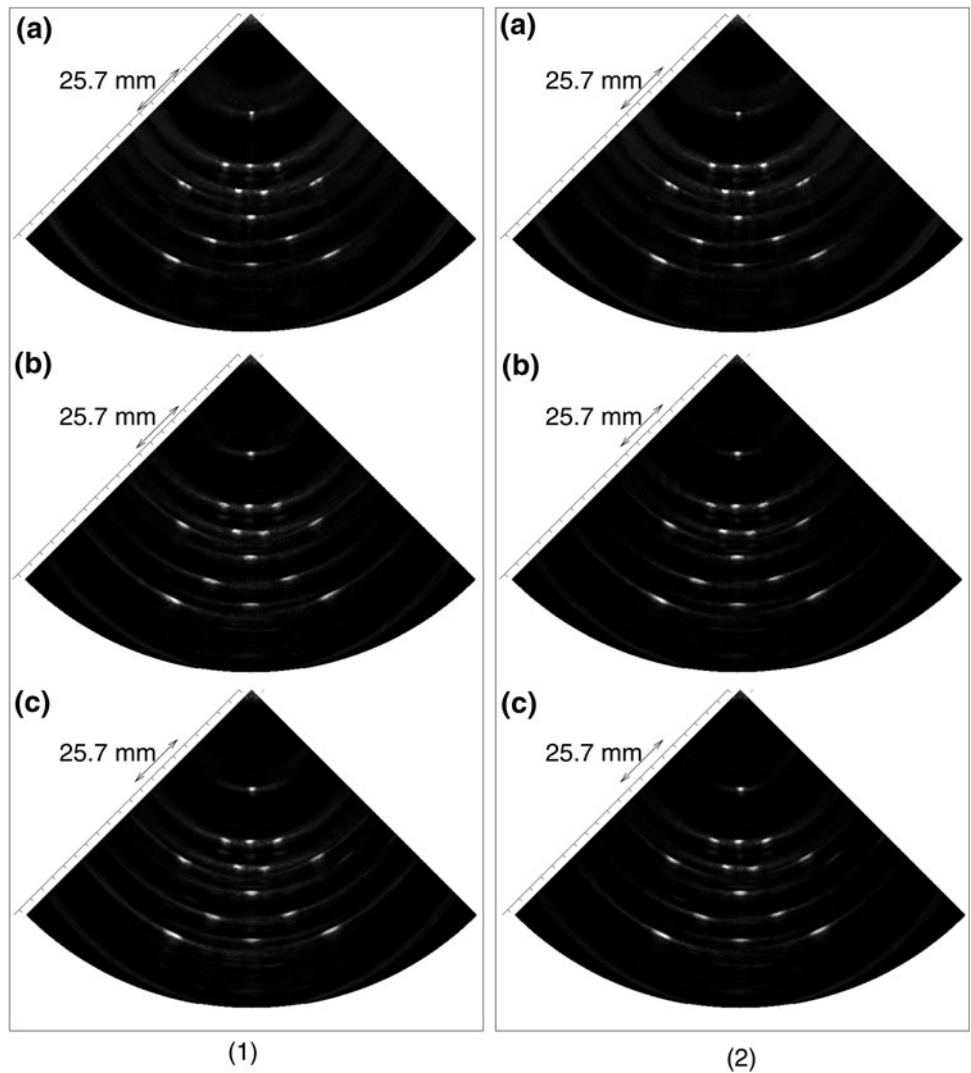


**Fig. 10** Lateral profiles of envelopes of beamformed RF echoes at range distance of 41 mm obtained by a diverging beam at  $r_f = 50$  mm with and without the limitation  $M_c \leq 2$

realize B-mode imaging in sector format based on parallel beamforming, spherically diverging waves were used in transmission.

In the present study, in receive beamforming, the propagation delay of the emitted diverging wave was calculated by considering the geometry of the transducer array and the virtual point source. However, increase of the number of compounded signals  $M_c$ , corresponding to increase of the transmission steering angle from the direction of interest  $\theta$ , degraded the resultant B-mode images. This would be caused by wavefront distortion of the emitted wave due to steering. In future work, methods for accurate realization of the desired wavefront or accurate calculation of the resultant wavefront will be necessary to increase the number of compounded signals for further improvements of image resolution, because the difference in angles of wavefronts in different transmissions would increase when using a greater number of transmissions for compounding, as illustrated in Fig. 8. In addition, phase aberration correction [26, 27] would be useful for receive beamforming.

Although diverging waves should be used to achieve a full lateral field of view of  $90^\circ$ , plane waves could be used

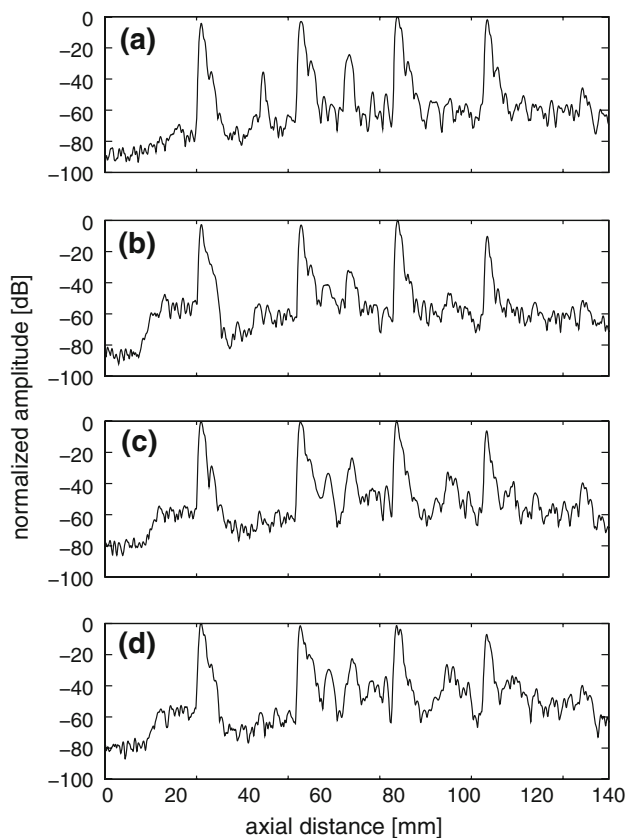


**Fig. 11** Axial profiles of the images of wires (shown in Fig. 6) at lateral angle of  $0^\circ$ . **a** Conventional beamforming (focusing in both transmit and receive). **b** Parallel beamforming with plane waves. **c** and **d** Parallel beamforming with diverging beams at  $r_f = 100$  and  $50$  mm, respectively

for imaging of a narrower region. Plane waves are more easily implemented in ultrasonic diagnostic equipment and make it easier to calculate the propagation delay of the wavefront. This was shown by the results in Fig. 9, where increase of the maximum number of compounded signals did not degrade the resultant B-mode image in the case of plane wave transmission. The error in the calculated propagation delay at larger steering angles was considered to be smaller for plane waves than for diverging waves. Figure 13 shows a longitudinal B-mode image of the heart of the same subject as in Fig. 12 obtained with plane wave transmission and smaller steering angles. As can be seen in Fig. 13, a B-mode image of good quality can be obtained at a very high frame rate (1010 Hz) that is much higher than that (200 Hz) achieved by conventional sector scanning with a narrow field of view [10].

The limitation of the hardware used in the present study is that it takes about 1 min to prepare for transmission of diverging waves. During this preparation, an operator needs to fix the position of the ultrasonic probe without viewing B-mode images. This limitation significantly increases the difficulties of in vivo measurements,

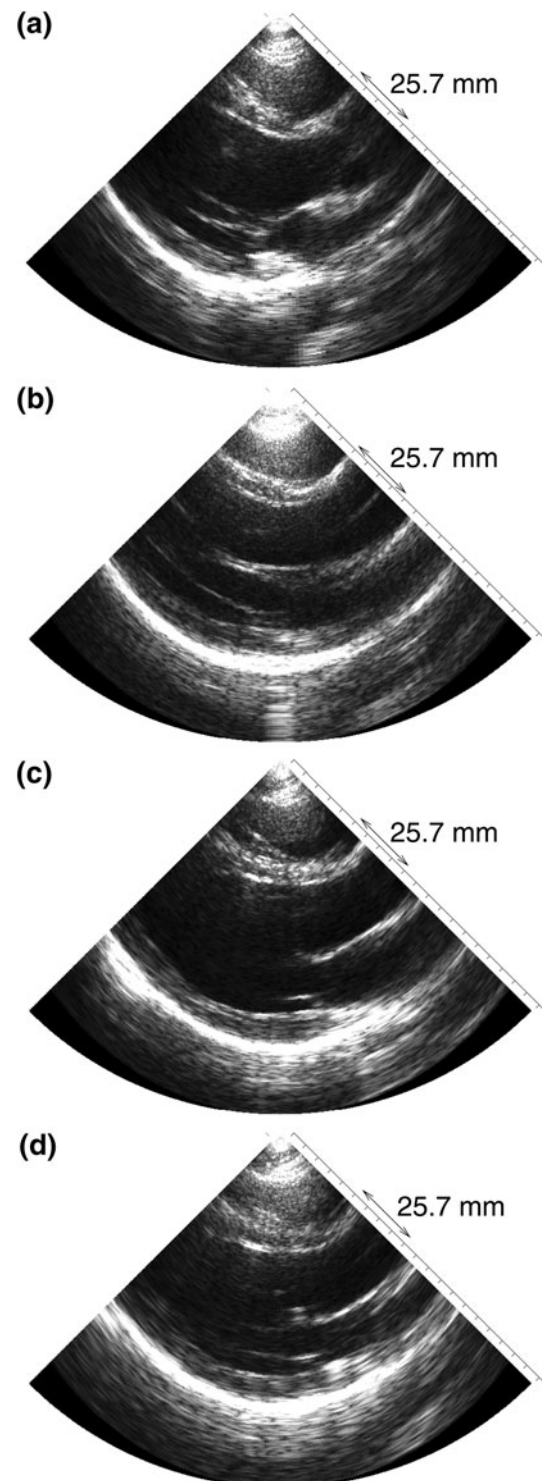


**Fig. 12** B-mode images of the heart of a 23-year-old healthy male obtained by **a** conventional sector scanning, and parallel beamforming using **b** plane waves, **c** diverging waves at  $r_f = 100$  mm, and **d** diverging waves at  $r_f = 50$  mm. The maximum number of compounded signals was limited to be 2 for diverging waves

particularly scanning of the same section several times. In future work, we need to develop a real-time system realizing the method proposed in the present study.

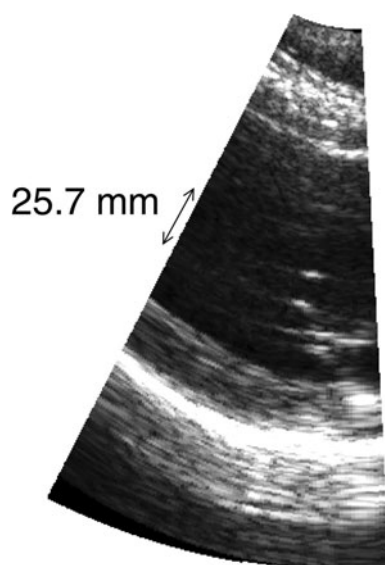


**Fig. 13** B-mode image of the heart of the same subject as in Fig. 12 obtained by parallel beamforming with plane waves and a smaller maximum steering angle (frame rate 1010 Hz)

## Conclusions

In this study, a method based on parallel beamforming and spatial compounding was proposed for high-frame-rate echocardiography. Although there was no significant degradation of axial or lateral spatial resolution, the lateral sidelobe levels increased. This increased sidelobe level degraded the contrast of the resultant B-mode image. However, a B-mode image of a heart could be obtained at a high frame rate of 316 Hz with a full lateral field of view of 90° and with image quality comparable to that obtained by conventional sector scanning. The image resolution achieved by the proposed method was much better than that obtained by sparse scanning [12], and the proposed method achieved a full lateral field of view without requiring ECG gating [11].

## References

1. Sutherland GR, Salvo GD, Claus P, et al. Strain and strain rate imaging: a new approach to quantifying regional myocardial function. *J Am Soc Echocardiogr*. 2004;17:788–802.
2. Sutherland GR, Stewart MJ, Groundstroem KW, et al. Color Doppler myocardial imaging: a new technique for the assessment of myocardial function. *J Amer Soc Echocardiogr*. 1994;7:441–58.
3. Heimdal A, Støylen A, Torp H, et al. Real-time strain rate imaging of the left ventricle by ultrasound. *J Am Soc Echocardiogr*. 1998;11:1013–9.
4. Yoshiara H, Hasegawa H, Kanai H, et al. Ultrasonic imaging of propagation of contraction and relaxation in the heart walls at high temporal resolution. *Jpn J Appl Phys*. 2007;46:4889–96.

5. Kanai H. Propagation of spontaneously actuated pulsive vibration in human heart wall and in vivo viscoelasticity estimation. *IEEE Trans Ultrason Ferroelectr Freq Control*. 2005;51:1931–42.
6. Kanai H. Propagation of vibration caused by electrical excitation in the normal human heart. *Ultrasound Med Biol*. 2009;35:936–48.
7. Bers DM. Excitation-contraction coupling and cardiac contractile force, 2nd ed. Dordrecht: Kluwer Academic Publishers;2001.
8. Konofagou E, Luo J, Fujikura K, et al. Imaging the electromechanical wave imaging of cardiovascular tissue in vivo. In: *Proceedings of IEEE Ultrasonics Symposium*; 2006. p. 985–8.
9. Konofagou EE, D'hooge J, Ophir J. Myocardial elastography—a feasibility study in vivo. *Ultrasound Med Biol*. 2002;28:475–82.
10. D'hooge J, Konofagou E, Jamal F, et al. Two-dimensional ultrasonic strain rate measurement of the human heart in vivo. *IEEE Trans Ultrason Ferroelectr Freq Control*. 2002;49:281–6.
11. Wang S, Lee W, Provost J, et al. A composite high-frame-rate system for clinical cardiovascular imaging. *IEEE Trans Ultrason Ferroelectr Freq Control*. 2008;55:2221–33.
12. Kanai H, Koiwa Y. Myocardial rapid velocity distribution. *Ultrasound Med Biol*. 2001;27:481–98.
13. Bradley C. Retrospective transmit beamformation. Whitepaper ACUSON SC2000™ Volume Imaging Ultrasound System. 2008.
14. Lu J. 2D and 3D high frame rate imaging with limited diffraction beams. *IEEE Trans Ultrason Ferroelectr Freq Control*. 1997;44:839–56.
15. Lu J. Experimental study of high frame rate imaging with limited diffraction beams. *IEEE Trans Ultrason Ferroelectr Freq Control*. 1998;45:84–97.
16. Cheng J, Lu J. Extended high-frame rate imaging method with limited-diffraction beams. *IEEE Trans Ultrason Ferroelectr Freq Control*. 2006;53:880–99.
17. Lu J, Cheng J, Wang J. High frame rate imaging system for limited diffraction array beam imaging with square-wave aperture weightings. *IEEE Trans Ultrason Ferroelectr Freq Control*. 2006;53:1796–812.
18. Shattuck DP, Weinschenker MD, Smith SW. Explososcan: A parallel processing technique for high speed ultrasound imaging with linear phased arrays. *J Acoust Soc Am*. 1984;75:1273–82.
19. Tanter M, Bercoff J, Sandrin L, et al. Ultrafast compound imaging for 2-D motion vector estimation: Application to transient elastography. *IEEE Trans Ultrason Ferroelectr Freq Control*. 2002;49:1363–74.
20. Hasegawa H, Kanai H. Simultaneous imaging of artery-wall strain and blood flow by high frame rate acquisition of RF signals. *IEEE Trans Ultrason Ferroelectr Freq Control*. 2008;55:2626–39.
21. O'Donnell M, Thomas LJ. Efficient synthetic aperture imaging from a circular aperture with possible application to catheter-based imaging. *IEEE Trans Ultrason Ferroelectr Freq Control*. 1992;39:360–80.
22. Karaman M, O'Donnell M. Synthetic aperture imaging for small scale systems. *IEEE Trans Ultrason Ferroelectr Freq Control*. 1995;42:429–42.
23. Hasegawa H, Kanai H. Fast ultrasonic imaging of the heart using spherically diverging beam. Technical Report of IEICE. 2010; 110:65–8.
24. Mahafza BR. Introduction to radar analysis. Boca Raton: CRC Press;1998.
25. Jespersen SK, Wilhjelm JE, Sillesen H. Multi-angle compound imaging. *Ultrason Imaging*. 1998;20:81–102.
26. Fortes JMP. A closed loop ML algorithm for phase aberration correction in phased array imaging systems—Part I: Algorithm synthesis and experimental results. *IEEE Trans Ultrason Ferroelectr Freq Control*. 1997;44:259–70.
27. Li Y. Phase aberration correction using near-field signal redundancy—Part I: Principles. *IEEE Trans Ultrason Ferroelectr Freq Control*. 1997;44:355–71.